ACS NANO
Cite This: ACS Nano XXXX, XXX, XXX–XXX
www.acsnano.org

ARTICLE

# Surface-Enhanced Molecular Electron Energy Loss Spectroscopy

Andrea Konečná,[†] Tomáš Neuman,[†] Javier Aizpurua,[*,†,‡] and Rainer Hillenbrand[*,¶,§]

[†]Materials Physics Center, CSIC-UPV/EHU, Donostia-San Sebastián, 20018, Spain
[‡]Donostia International Physics Center DIPC, Donostia-San Sebastián, 20018, Spain
[¶]IKERBASQUE, Basque Foundation for Science, Bilbao, 48013, Spain
[§]CIC NanoGUNE and UPV/EHU, Donostia-San Sebastián, 20018, Spain

Supporting Information

**ABSTRACT:** **Electron energy loss spectroscopy (EELS) in a scanning transmission electron microscope (STEM) is becoming an important technique in spatially resolved spectral characterization of optical and vibrational properties of matter at the nanoscale. EELS has played a significant role in understanding localized polaritonic excitations in nanoantennas and also allows for studying molecular excitations in nanoconfined samples. Here we theoretically describe the interaction of a localized electron beam with molecule-covered polaritonic nanoantennas, and propose the concept of surface-enhanced molecular EELS exploiting the electromagnetic coupling between the nanoantenna and the molecular sample. Particularly, we study plasmonic and infrared phononic antennas covered by molecular layers, exhibiting either an excitonic or vibrational response. We demonstrate that EEL spectra of these molecule-antenna coupled systems exhibit Fano-like or strong coupling features, similar to the ones observed in far-field optical and infrared spectroscopy. EELS offers the advantage to acquire spectral information with nanoscale spatial resolution, and importantly, to control the antenna-molecule coupling on demand. Considering ongoing instrumental developments, EELS in STEM shows the potential to become a powerful tool for fundamental studies of molecules that are naturally or intentionally located on nanostructures supporting localized plasmon or phonon polaritons. Surface-enhanced EELS might also enable STEM-EELS applications such as remote- and thus damage-free-sensing of the excitonic and vibrational response of molecules, quantum dots, or 2D materials.**

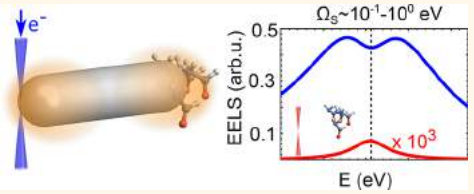


**KEYWORDS:** *electron energy loss spectroscopy, plasmonic antennas, Fano resonances, strong coupling, surface-enhanced spectroscopy*

Electronic transitions and vibrations are key excitations in matter that allow for characterizing and identifying materials. A variety of external probes, such as photons or electrons, can be used to effectively interact with matter in the eV and meV energy ranges, respectively, providing information on electronic and vibrational properties of bulk materials, two-dimensional layers,[1,2] organic molecules,[3,4] quantum dots,[5,6] and topological structures,[7] among others. In this context, organic molecules have often been studied by techniques such as fluorescence spectroscopy, which provides information on the occupied and unoccupied molecular orbitals,[8] as well as on the lifetime of the excited electronic states.[9] On the other hand, the spectral information on molecular vibrations is typically accessed via the analysis of inelastically scattered light (Raman scattering),[10] or from direct absorption of infrared light.[11] However, the direct interaction of light and matter, as used in the aforementioned techniques, is often weak, and little or no signal can be obtained from small amounts of molecular samples. To overcome this limitation, metallic surfaces and nanostructures—acting as efficient optical and infrared nanoantennas—have been exploited to concentrate the electromagnetic field in the proximity of target molecules, thus producing a dramatic enhancement of their spectroscopic response.[12] These so-called surface-enhanced spectroscopy techniques rely on the electromagnetic near-field coupling of surface plasmons and matter excitations.[13] For instance, surface-enhanced molecular fluorescence[14] has revealed interference in a single emitter's fluorescence due to surface plasmon-exciton interaction, surface-enhanced Raman scattering (SERS) has allowed optical mapping of the vibrational fingerprints of a single molecule in a plasmonic cavity,[15] and surface-enhanced infrared absorption (SEIRA) has provided vibrational information on a few thousands of molecules on metallic infrared nanoantennas.[16−19]

The interaction between plasmons in an optical antenna and molecular excitations can be so efficient that the "strong coupling regime" can be reached under certain circumstances. In molecular fluorescence, for example, the strong coupling

Received: February 25, 2018
Accepted: April 11, 2018
Published: April 11, 2018




DOI: 10.1021/acsnano.8b01481
ACS Nano XXXX, XXX, XXX–XXX

regime is reached when the interaction rate between the antenna plasmon and the molecular exciton is faster than the decay rate of both plasmon and exciton, leading to the creation of new hybrid plasmon–exciton polaritonic states.[20−23] Thus, plasmon–exciton coupling offers intriguing possibilities to tailor molecular states for controlling chemical reactivity or for quantum information processing.[24] Strong coupling phenomena have been studied by optically exciting plasmons and excitons, for example, in organic dyes forming J-aggregates[25−31] or in quantum dots.[32−36] Recently, the concept of strong coupling has also been explored in the infrared spectral range, where the electromagnetic fields of phonon polaritons in hexagonal boron nitride (h-BN) antennas[37,38] were coupled to infrared-active vibrations of molecules deposited on top of the antennas.[39]

Here we propose EELS in STEM[40] for studying the coupling between plasmons and molecular excitations (both electronic excitations and vibrations) with nanoscale spatial resolution. Moreover, we propose the use of plasmonic and infrared-phononic antennas to enhance EELS signals from optical excitonic and infrared vibrational excitations. We coin this spectroscopic scheme as "surface-enhanced EELS", analogously to its optical counterpart.

EELS employing a tightly focused electron beam has enabled the correlation of the local spectral response with atomic scale imaging,[41] thereby relating the optical properties of a sample with its precise shape and structure. EELS in STEM has been successfully used, for instance, in characterization and mapping of localized surface plasmon (LSP) polaritons[42−45] or even coupled LSPs[46−52] in the optical spectral range. Moreover, recent advances in instrumentation have dramatically improved the spectral resolution in EELS,[53−55] opening access to the very low-energy loss range, where not only optical but also infrared excitations can be explored. This recent improvement has thus enabled to probe vibrational excitations and surface phonon polaritons.[54−,59] This has turned EELS into a powerful technique for spatial characterization of low-energy excitations in matter, which can be employed at both VIS and IR frequencies, owing to the broadband nature of the electromagnetic field of the probing electron.

In this work, we present a comprehensive numerical and analytical study of molecular excitations in STEM-EELS, which are enhanced by plasmonic and phononic nanorods, acting as effective nanoatennas. We first demonstrate the mechanism of antenna-molecule coupling probed by the electron beam in the visible spectral range. Specifically, we analyze the response of an excitonic molecular layer covering antennas exhibiting dipolar and dark plasmonic antenna modes, revealing that strong coupling can emerge and can be probed by EELS. In analogy to SEIRA, we also study EELS of IR plasmonic and phononic antennas coupled to IR active molecules. Furthermore, we provide details on the decay of the enhanced signal as a function of the distance between the beam and the antenna. We demonstrate the possibility of using surface-enhanced EELS for (ultra)remote molecular sensing, completing the set of advantages that the proposed technique offers.

## RESULTS AND DISCUSSION

**Principle of Surface-Enhanced EELS.** We begin our study by describing the general features appearing in EELS of a plasmonic rod interacting with molecules. The considered model system is sketched in Figure 1a. It consists of a plasmonic antenna fully or partially covered by a molecular layer (sample), which is a system typically studied in optical and infrared spectroscopy. We choose a simple and highly tunable antenna shape: a silver nanorod of variable length $L$ and with rounded tips of radius $R$ = 20 nm. The molecular layer thickness is $t$ = 5 nm. We consider the coupling of a 60-keV electron beam with the longitudinal antenna modes,[48,51,60−62] whose energy can be tuned by varying the antenna length to match the energy of the molecular excitons (relatively short plasmonic antennas) or molecular vibrations (relatively long plasmonic antennas) of the layer. For simplicity, the dielectric response is approximated by the Drude model for silver and by the Lorentz–Drude dielectric function in the case of the sample (see Methods). Electron energy loss probability spectra are calculated numerically within the framework of classical dielectric theory[63,64] as specified in the Methods.

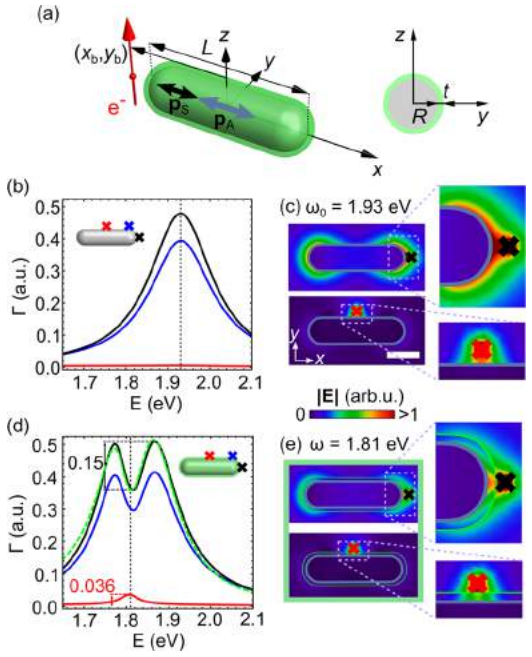


**Figure 1. (a) Schematic of the modeled system: a silver rod of length $L$ and radius $R$ = 20 nm covered with an excitonic layer of thickness $t$ = 5 nm. It is probed by an electron beam passing at a position $(x_b,y_b)$, which is called the impact parameter. (b) EEL spectra [given in Hartree atomic units (a.u.)] of a bare silver antenna of length $L$ = 145 nm. Black, blue, and red spectra are obtained for the beam passing at $(L/2 + 10$ nm, 0), $(L/2 - R, R + 10$ nm) and (0, $R + 10$ nm), respectively. (d) Spectra for the same beam positions as in panel b, but for the rod fully covered by an excitonic layer as shown in the inset. The green dashed curve is the coupled-dipole model fit using eq 1. We further denote the spectral contrast, defined as the dip depth or peak height. In panels c and e, we plot the total electric field magnitude |E| in the plane $z$ = 0 for the bare and the covered rod, respectively (color scale is the same for all field plots). Blue and red crosses mark the electron beam position. The scale bar is 50 nm. The rod and the layer boundaries are marked by gray and green lines, respectively.**

To better understand the EEL spectra of the antenna–molecule system, we first analyze the interaction of the bare antenna with the probing electron beam. To that end, we calculated EEL spectra (Figure 1b) at the different electron beam positions marked by crosses in the inset. When the beam is close to the tip of the antenna (black and blue cross), a single peak at energy $\omega_0$ = 1.93 eV with a full width at half-maximum (fwhm) of 187 meV can be observed (black and blue spectra in


DOI: 10.1021/acsnano.8b01481
ACS Nano XXXX, XXX, XXX−XXX

Figure 1b). The peak disappears when the beam is placed closer to the center of the antenna, at $x_b$ = 0 nm (red spectrum). To understand the excitation at $\omega_0$, we plot the total near field (external field of the electron plus the induced field) associated with the different beam positions in Figure 1c. When the beam is placed at the antenna apex (upper panel of Figure 1c), we observe a near-field pattern corresponding to the longitudinal dipolar plasmonic mode (charge oscillates along the longer antenna axis). On the contrary, when the e-beam is placed near the center of the rod (lower panel of Figure 1c), it does not excite the dipolar antenna resonance, and the near-field distribution is thus dominated by the external field of the electron.[44,60,62] The low excitation efficiency can be explained by the negligible near-field magnitude of the longitudinal dipolar mode near the rod center. However, we note that higher order antenna modes as well as transverse modes (with charge oscillating along the short antenna axis) can be excited at energies above 3 eV (see Supporting Information Figure S1).

Next we cover the rod by an excitonic molecular layer, which is modeled by the following parameters: $\varepsilon_{\infty,s}$ = 1.69, $\omega_s$ = 1.8 eV, $\gamma_s$ = 50 meV and $f_s$ = 0.02 (eq 3 of Methods) mimicking the case of J-aggregates in solution.[22,27,29] Analogously to the case of the bare antenna, we show EEL spectra in Figure 1d for different e-beam positions. When the beam is positioned close to the antenna apex, we efficiently excite the antenna mode and the resulting EEL spectrum exhibits the response of the coupled antenna−molecule system (black, blue). We recognize the coupling signature in the form of a typical Fano-like feature (dip),[16] which reveals the coherent interaction between the antenna and the molecular sample. Moreover, the antenna resonance is slightly red-shifted due to the dielectric screening by the molecular layer ($\varepsilon_{\infty,s}$). The field plot at energy $\omega$ = 1.81 eV (upper panel of Figure 1e) shows the dipolar near-field pattern surrounding the antenna, revealing the regions of intense field where the electromagnetic coupling between the antenna near fields and the molecular layer takes place.[29,65]

When the beam is positioned closer to the antenna center, the dipolar plasmon is not efficiently excited, and we thus probe the decoupled excitonic sample. The excitonic response appears in the form of a small narrow peak in the spectrum (red curve in Figure 1d). By defining the spectral contrast as the depth of the dip of the coupled system and as the height of the spectral peak of the uncoupled exciton (marked by black and red vertical arrows in Figure 1d), we can estimate the antenna-induced enhancement of the exciton's spectral feature compared to the bare exciton spectrum. From the black and red spectra in Figure 1d we find that the contrast is, without further optimization, more than four times enhanced in the coupled system (0.15 compared to 0.036).

To better understand the underlying physics and to explain the numerically calculated spectral shapes, we developed an analytical model of the response of the coupled system, described as a combination of two electromagnetically coupled dipoles representing the antenna $\mathbf{p}_A$ and the sample $\mathbf{p}_S$, respectively, excited by the external field of the aloof electron beam (see schematics in Figure 1a). Within the framework of this model (see Methods for a detailed derivation), we find an analytical expression for the electron energy loss probability:

$$\Gamma \approx \Gamma_A + \Gamma_{AS} = \frac{1}{\pi}\mathrm{Im}\left[\frac{\alpha_A (E_x^A)^2}{1-\alpha_A\alpha_S G^2}\right] + \frac{1}{\pi}\mathrm{Im}\left[\frac{2\alpha_A G \alpha_S E_x^A E_x^S}{1-\alpha_A\alpha_S G^2}\right] \quad (1)$$

where $E_x^{A/S}$ is the $x$ component of the electric field of the electron at the antenna/sample position. $\alpha_{A/S}$ are the polarizabilities of antenna and sample, and $G$ is the relevant component of the dyadic Green's function (in our case the $xx$ component), describing the electromagnetic interaction between the antenna and the sample. A representative fit of the coupled dipole model (eq 1) for a situation with the beam position close to the antenna apex (black) is shown by the green dashed curve in Figure 1d, yielding excellent agreement with the numerical result (see Methods for the fitting details).

We note that the loss probability as given by eq 1 (except for prefactors), formally provides the same spectral shape as the optical extinction of the coupled system.[17,65] Importantly, we find that the expression for $\Gamma$ in eq 1 contains two contributions to the EEL signal represented by the terms $\Gamma_A$ and $\Gamma_{AS}$. $\Gamma_A \propto (E_x^A)^2$ arises from the effective polarizability of the antenna that is modified by the presence of the molecular sample, and is usually the dominant contribution. On the other hand, $\Gamma_{AS} \propto E_x^A E_x^S$, represents the losses in the sample due to the field generated by the antenna, and vice versa. $\Gamma_{AS}$ is small compared to $\Gamma_A$ when $2\alpha_S G E_x^S < E_x^A$. However, when the electron beam excites the sample with high efficiency (*e.g.*, when it is close to the sample, $E_x^S \gg E_x^A$), the indirect term $\Gamma_{AS}$ becomes important and leads to asymmetries in the EEL spectra beyond the Fano-like model. For further comparison we provide the calculated optical spectra in Figure S2.

**Exploiting Higher-Order Plasmonic Modes for Surface-Enhanced EELS.** An important advantage of fast electrons in EELS is their ability to probe "dark" plasmonic modes, which do not efficiently radiate into the far field. These modes are thus hardly detectable by far-field optical spectroscopy in conventional experimental arrangements, but become accessible by a localized probe, such as the electron beam in EELS experiments.[45−47,50] The damping of dark modes is mainly caused by the intrinsic absorption of the material (ohmic losses), with radiation losses largely suppressed. The reduced losses of dark modes thus facilitate reaching the strong coupling regime, where the rate of the molecule−antenna interaction needs to be faster than the loss rate of excitons and plasmons in the system.[20] Moreover, the coupling strength typically increases when the plasmonic near field is more confined (the latter corresponding to a decrease of the effective mode volume),[66] a situation more likely to occur for dark modes. Strong coupling has recently attained a large interest, for example, because of the possibility to modify the chemical reactivity of molecules.[67−69] In the following we thus study the coupling of dark antenna modes and molecular excitons with an electron-beam.

We performed calculations similar to those in Figure 1 for a longer antenna of length $L$ = 340 nm, which exhibits the second order longitudinal mode (first dark one) tuned with respect to the energy of the excitonic transition. In Figure 2a we show spectra obtained for three different positions (marked by crosses in the inset) of the electron beam along the antenna. The dark mode is excited when the beam is positioned either close to the antenna center or close to the antenna tips (red and black spectra, respectively). Note that the loss peak with a fwhm of 63 meV is much narrower than the loss peak associated with the dipolar mode in Figure 1b, which, as mentioned above, is due to the suppression of radiation losses (reduced damping). The near-field plots for each beam position at $\omega_0$ = 1.89 eV (Figure 2b) confirm the excitation of the second order antenna mode (three bright spots corresponding



DOI: 10.1021/acsnano.8b01481
ACS Nano XXXX, XXX, XXX−XXX

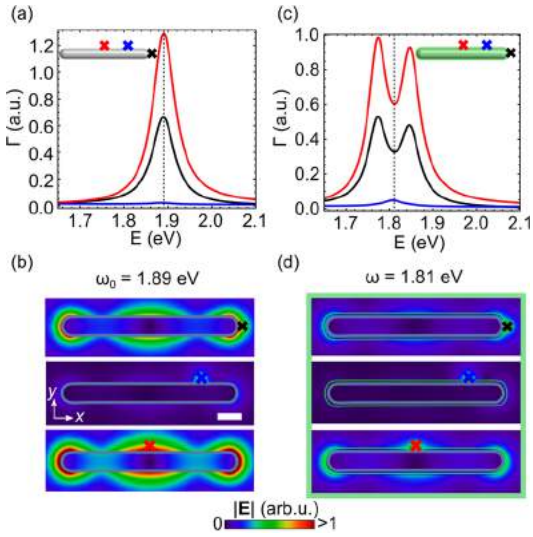


**Figure 2. (a) EEL spectra of the bare silver antenna of length $L$ = 340 nm for the electron beam passing at ($L$/2 + 10 nm, 0) (black), ($L$/4, $R$ + 10 nm) (blue), and (0, $R$ + 10 nm) (red). (c) Spectra at the same beam positions for the rod covered by the excitonic layer (see the inset). In panels b and d we plot the total electric field magnitude |E| in the plane $z$ = 0 for the bare rod and the covered rod, respectively, and the electron beam positions marked by the colored crosses. The scale bar is 50 nm. The rod and the layer boundaries are marked by gray and green lines, respectively.**

to the localized plasmonic mode). The mode is not excited when the beam is positioned at one of the two nodes (dark areas). Subsequently the excitation probability is close to zero (blue curve in Figure 2a).

The coupling of the dark plasmon mode and the excitonic layer covering the plasmonic rod is demonstrated in the spectra of Figure 2c, which are calculated for the same beam positions as in Figure 2a. The coupling signatures emerge for positions of the beam, where it efficiently excites the plasmonic mode, that is, close to the antenna center or at apexes (red and black spectra). On the contrary, when the beam is placed at the node, we probe the uncoupled exciton (blue spectrum), analogously to the centered e-beam in the dipolar plasmonic antenna (red curve in Figure 1d). The field patterns at $\omega$ = 1.81 eV for the covered antenna (Figure 2d) show similar features as those in Figure 2b for the corresponding beam positions, although less intense due to field screening by the molecular layer. These near-field maps reveal the areas of maximum enhancement, in which the most effective coupling with the sample takes place. The spectra for the beam at the antenna center and apexes (red and black curves in Figure 2c) therefore show the coupled system response.

Interestingly, the coupling between the dark antenna mode and the molecular exciton seems to be more pronounced than for the bright dipolar mode. However, for a fair comparison, a quantitative analysis of the coupling in both cases is needed. To that end, we calculated a set of energy loss spectra for varying antenna lengths around the first order (dipolar) and the second order (first dark) antenna modes. The results are shown in Figure 3a and 3b, respectively. As the antenna resonance is detuned with respect to the exciton, we observe in both cases two peaks which change intensity and energy position. For highly detuned antennas, the peaks correspond to the uncoupled exciton and plasmon excitations (their energy positions are traced by green and black solid lines), respectively.

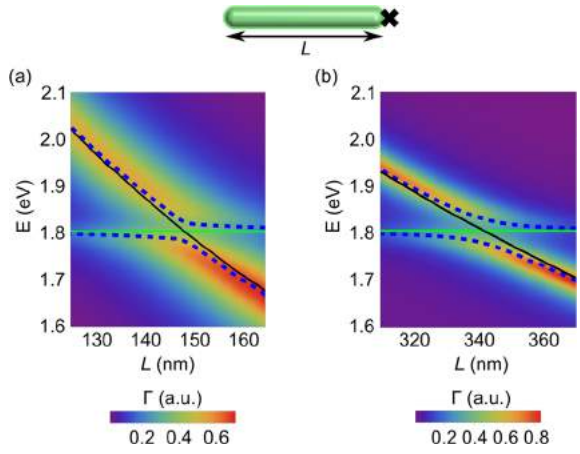


**Figure 3. EEL spectra calculated for rods with varying lengths supporting (a) the first order (bright) dipolar mode and (b) the second order (dark) dipolar mode excitation. The electron beam is placed at ($L$/2 + 10 nm, 0) as sketched in the schematic. The blue dashed lines show the coupled oscillator fit described in the Methods, the black line marks the EEL maxima calculated for the bare rods, and the green line marks the EEL peak of the bare excitonic layer.**

When the plasmon resonances approach the exciton (around $L$ = 150 and 340 nm), we see a typical anticrossing of the two peaks,[22] which is a manifestation of either weak or strong coupling.

To determine the coupling regime, we use the coupled dipole model introduced above to obtain the energies of the two new eigenmodes of the coupled system arising from the interaction (for details see Methods), similarly as performed previously in the analysis of optical spectra.[24,29,31,70] The mode energies obtained from the fit are shown as dashed blue lines in Figure 3. They closely trace the peak maxima. From a quantitative evaluation (see Methods), we find that the excitonic sample coupled with the dipolar plasmonic antenna is in the weak coupling regime (which is also verified by the absence of the double peak structure in the optical absorption calculated inside the excitonic layer,[22,71] see Figure S2). However, we reach strong coupling with the use of the first dark mode. In this case, the smaller damping of the plasmonic mode is crucial to achieve this interaction regime.

Additional simulations and analyses (Figures S2 and S3 of Supporting Information) show that strong coupling can be also achieved when the third and fourth order plasmon resonance match the excitonic resonance. The possibility to probe simultaneously both the coupled antenna–molecule system and the uncoupled molecular sample, as shown here, turns EELS into a promising tool for fundamental studies of strong coupling between plasmons and excitons.

**Surface-Enhanced Vibrational Spectroscopy with EELS.** Our concept to study the coupling of molecules with antennas in EELS is general and does not apply only to plasmon–exciton systems. Plasmonic antennas can exhibit resonances in widely different spectral ranges, including the mid-infrared spectral range (50 to 500 meV) where molecular vibrations occur. Both mid-infrared plasmons and molecular vibrations can be well accessed by recently developed EELS instrumentation.[53,54] Interestingly, the mid-infrared spectral range also hosts phonon polaritons in polar crystals (*e.g.*, SiC, MgO, quartz)[72] and van der Waals materials (*e.g.*, h-BN).[37,73] Recent experimental studies demonstrate that SiC and h-BN


DOI: 10.1021/acsnano.8b01481
ACS Nano XXXX, XXX, XXX–XXX

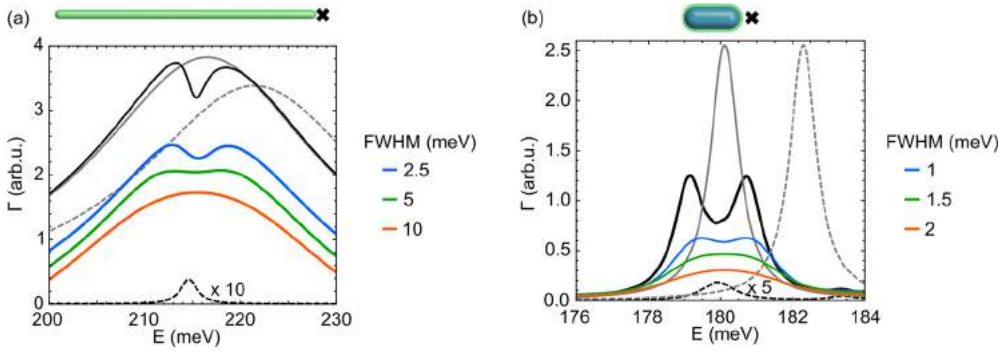


**Figure 4. (a) EELS of a silver wire with length $L$ = 1910 nm covered by a PMMA layer, excited by an electron beam passing at ($L$/2 + 10 nm, 0). The simulated spectrum (black) is convolved with a Gaussian function of fwhm 2.5/5/10 meV (blue/green/orange). (b) h-BN antenna of length $L$ = 102 nm covered by a layer of CBP molecules is probed by an electron beam passing at position ($L$/2 + 10 nm, 0). The calculated spectrum (black) is convolved with a Gaussian function of fwhm 1/1.5/2 meV (blue/green/orange). The convolved spectra are scaled and vertically shifted for better readability.**

phonon polariton resonators (in the following referred as to IR-phononic antennas) exhibit mid-infrared resonances of quality factors much higher than that of plasmonic antennas,[39,72,74] which can be accessed by EELS as well.[59,75] The coupling of molecules and well-defined phononic antennas has been only very recently demonstrated by infrared far-field spectroscopy of molecules-covered h-BN ribbons, reaching even the strong coupling limit.[39] In the following, we thus explore the potential of surface-enhanced EELS of molecular vibrations in the IR spectral range employing plasmonic and phononic antennas.

We first study the EEL spectra of a long silver wire (exhibiting mid-IR plasmon resonances) covered by a thin poly(methyl methacrylate) (PMMA) layer. PMMA exhibits a rich infrared absorption spectrum, but we focus on the interaction of the plasmons with the carbonyl (C═O bond) stretching mode. The carbonyl stretching vibration is well characterized by a Lorentz oscillator (according to eq 3 of Methods) with $\varepsilon_{\infty,s}$ = 2.12, $\omega_s$ = 214.4 meV, $\gamma_s$ = 2 meV, and $f_s$ = 0.0136, and produces the weak peak in the EEL spectrum calculated only for the PMMA layer (black dashed curve in Figure 4a). We consider an antenna of lenght $L$ = 1910 nm. The spectrum for the bare antenna is shown in Figure 4a by the gray dashed curve. The spectrum of the antenna covered with a dielectric layer characterized by $\varepsilon_s = \varepsilon_{\infty,s}$ = 2.12 is shown by the gray line. When the molecular layer is placed on top of the antenna, we clearly see a Fano-like vibrational feature in the IR EEL spectrum (solid black curve), similar to SEIRA spectra (see Figure S4a). However, the experimental detection of vibrational fingerprints in EELS is still challenging because of the limited spectral resolution caused by the finite width of the zero-loss peak.[54] We thus consider the finite experimental energy resolution, by convolving the calculated spectra with a Gaussian function whose fwhm corresponds to the instrumental resolution. In Figure 4a we compare the calculated EEL spectrum for the coupled system (black curve, zero-loss peak width is zero) with those where convolution was applied. The colored spectra display the results for zero-loss peak widths of 2.5, 5, and 10 meV. Our results show that (in the absence of experimental noise) a spectral resolution of at least 5 meV or better is required to resolve the spectral features associated with the molecular vibrations.

In Figure 4b we study surface-enhanced EELS based on IR-phononic antennas. We consider a similar system as in ref 39: a h-BN rod covered by a layer of 4,4′-bis(*N*-carbazolyl)-1,1′-biphenyl (CBP) molecules. The CBP molecules are characterized by their experimental dielectric response,[76] giving rise to an intense vibration at 180 meV (see EEL spectrum for the uncoupled CBP shell shown by the black dashed curve in Figure 4b). The h-BN antenna of length $L$ = 102 nm supports a dipolar localized phonon polariton mode, which produces a narrow EEL peak (gray dashed curve in Figure 4b), shifted to lower energies when the antenna is covered by a nonresonant dielectric layer (mimicking the molecular layer without absorption resonance) with $\varepsilon_s = \varepsilon_{\infty,s}$ = 2.8 (gray continuous curve). The EEL spectrum of the antenna covered by the molecules (black curve) shows a pronounced peak splitting and we find that the system is strongly coupled (see Figure S4b). By comparing the solid black spectra in Figure 4a,b, we can immediately see the difference between the weak perturbation of the plasmonic antenna response by coupling with the molecules (Figure 4a) and the emergence of the two hybridized modes when the CBP molecules are coupled with the h-BN antenna (Figure 4b). Convolution of the spectrum for the strongly coupled system in Figure 4b predicts that an instrumental resolution of 1 meV is required to resolve both peaks. Although such resolution is challenging even for state-of-the-art EELS instruments, we envision that emerging developments could allow for an experimental observation of this effect in the near future. We also note that the observation of plasmon-exciton coupling in the visible spectral range requires a spectral resolution of about 50 meV (see Figure S6), which is readily available with modern instrumentation.[53,77]

**Signal Decay.** The coupling of molecular excitations with plasmonic antennas enables the acquisition of information on the molecules through the plasmonic field. However, this field significantly extends the particle boundaries (see *e.g.*, Figure 1c), which implies that the spatial resolution in plasmon-enhanced EELS should be diminished compared to EELS of bare molecular samples. To explore this aspect, we performed EELS calculations for molecule-covered plasmonic and IR-phononic antennas for various electron beam positions in aloof geometry, that is, when the beam passes the molecule-covered antenna at a distance $b$ > 0 nm where $b$ = 0 defines the antenna boundary (see schematics in Figure 5).

We first analyze the EEL spectra as a function of distance $b$ for a plasmonic antenna in the visible spectral range. To that end, we choose the same system parameters as in Figure 1d. We find that the electron energy loss probability (solid lines in Figure 5a) for distances up to $b$ = 30 nm is still larger than in the case of the bare excitonic shell (dashed lines; the bare


DOI: 10.1021/acsnano.8b01481
ACS Nano XXXX, XXX, XXX−XXX

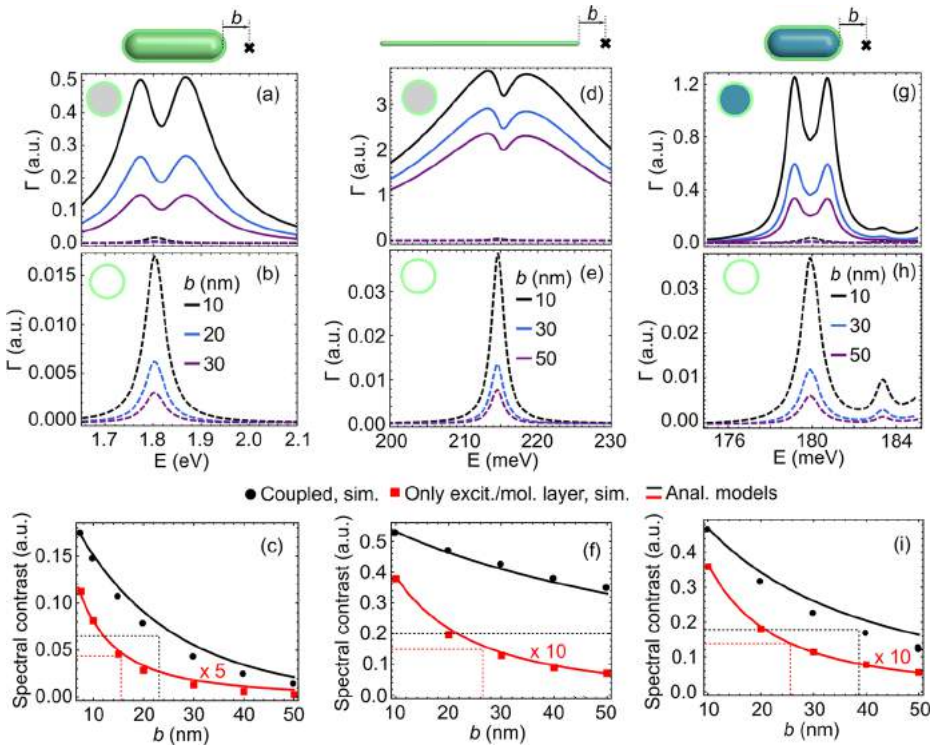


**Figure 5. (a,b) Full lines: Calculated EEL spectra for a silver rod ($L$ = 145 nm) covered by an excitonic layer and for the impact parameters ($L/2$ + $b$,0), where the distance of the electron beam from the particle boundary $b$ is 10 nm (black), 20 nm (blue), and 30 nm (purple). Dashed lines: calculation without the silver wire, zoomed in panel b. (c) EELS spectral contrast for the coupled scenario (black) or for the molecular response (red, multiplied by factor 5) as a function of $b$. The symbols show numerically calculated data, continuous lines represent analytical models. (d,e) Calculations analogous to (a,b), performed for a silver wire ($L$ = 1910 nm) covered by PMMA layer and for $b$ 10 nm (black), 30 nm (blue), and 50 nm (purple). (f) Analogous to panel c, evaluated for the IR wire. The molecular peak height is multiplied by factor 10. (g,h) Calculations analogous to (a,b), performed for the coupled system of h-BN antenna ($L$ = 102 nm) and CBP molecular shell, the dashed lines are for uncoupled CBP shell. The impact parameters are the same as in panels d and e. (i) Analogous to (c,f), evaluated for the coupled h-BN antenna−CBP molecular shell. The dashed lines in panels c, f, and i denote for which value of $b$ the spectral contrast drops to $1/e$ of its maximal value.**

excitonic EEL spectra are zoomed in Figure 5b for better visibility). For a quantitative analysis, we extract the spectral contrast (defined as the difference between the local maximum and minimum in the spectral region of the Fano feature, as marked in Figure 1d) from the EEL spectra in Figure 5a and plot it as a function of the distance $b$ in Figure 5c (black dots). We find that the spectral contrast of the coupled system decays less quickly with $b$ than that of the bare excitonic shell (defined as the peak height in Figure 5b; shown by red squares in Figure 5c). Furthermore, the coupling of the molecular excitons to the plasmon yields a more than 5-fold contrast enhancement.

We performed the same analysis for the long PMMA-covered silver wire at mid-infrared energies (same as in Figure 4a). The results are shown in Figures 5d,f. The solid curves in Figure 5d display the EEL spectra of the PMMA-covered wire, while the dashed curves in Figure 5d,e show the EEL spectra of the bare PMMA shell. The spectral contrast in Figure 5f is more than 10 times larger when the PMMA vibrations are coupled to the plasmons in the wires (black dots vs red squares, respectively). Importantly, the decay of the spectral contrast is much less pronounced for the PMMA shell coupled to the antenna fields (black dots) compared to the pure PMMA shell (red squares), allowing for detection of the PMMA vibrational EEL signal at much larger impact parameters, which could help to reduce sample damage induced by the electron beam.

Finally, we present in Figure 5g the calculated EEL spectra of an IR-phononic h-BN antenna covered by the CBP molecular layer (same as in Figure 4b). All spectra calculated for the coupled system (solid lines) exhibit clear peak splitting and higher loss probability than for the uncoupled CBP shell (dashed lines in Figures 5g,h). The spectral contrast for the coupled scenario is also more than 10 times higher and slightly slower decaying compared to the uncoupled CBP shell, as shown in Figure 5i.

We now compare and analytically model the spatial decay of the spectral contrast plotted in Figures 5c,f,i both in the uncoupled and coupled scenarios. The uncoupled molecular shell is excited only in a small volume close to the beam (see Figure 1e and also Figure S7), and thus can be replaced by an effective point dipole. The corresponding expression for the analytical decay (see details in Methods and eq 13 therein) shown by the red curves is in excellent agreement with the data points (red squares) obtained from the numerical simulations. Note that the signal decay length depends inversely on the energy of the excitations, which is a consequence of the spatial decay of the electromagnetic field of the electron beam (see eq 6 of Methods). The decay length is thus larger for molecular vibrations (Figure 5f,i) compared to visible excitons (Figure 5c).

We next compare the contrast decay for the molecules coupled with the antennas. As pointed out above, we find that the decay length is larger than without the antenna for each case (compare black and red dots in Figure 5c,f,i). Furthermore, we find significant differences in the decay



DOI: 10.1021/acsnano.8b01481
ACS Nano XXXX, XXX, XXX−XXX

considering the IR plasmonic and phononic antennas. As the spatial dependence of the spectral contrast for the coupled antenna–molecule system (black dots in Figure 5c,f,i) closely follows the strength of the bare antenna excitation as a function of $b$ (see Figure S8 and eq 12 of Methods), we can explain the results of our simulations by modeling the contrast decay of the corresponding uncovered antennas. The short plasmonic and phononic antennas can be replaced by point dipoles, positioned at the center of mass of the antennas and polarized along the $x$ direction (see eq 14 in Methods). The modeled decay is shown by the black curves in Figure 5c,i, reasonably reproducing the simulated results (symbols). However, the charge induced in the long IR plasmonic antenna is better described by considering a finite surface charge distribution of the plasmonic excitation,[78] which yields the EEL intensity decay (see eq 15 of Methods) shown by the black curve in Figure 5f, which is in good agreement with the simulated data (symbols).

By comparing the black curves in Figure 5f,i, we can conclude that the near field of the IR plasmonic antenna is spatially much more extended (less confined) compared to the IR phononic antenna. This occurs because the plasmon polariton wavelength is much larger than the phonon polariton wavelength, even though both IR antennas exhibit the fundamental resonance at similar energies. We thus emphasize that the nature of the polaritonic excitation as well as the particular charge distribution and shape of the antenna strongly influence the observed spectral contrast decay.[79]

**Ultraremote Sensing with EELS.** An interesting aspect of the use of plasmonic and IR-phononic antennas and nanostructures in EELS is the possibility to probe molecular excitations remotely, that is, in aloof geometry but with enhanced sensitivity. We explore this possibility for probing excitons in smaller amounts of molecules covering plasmonic antennas. To that end, we study a plasmonic silver rod with an excitonic molecular cap placed at only one of the antenna apexes (see schematic in Figure 6a). To match the energy of the dipolar plasmon with the exciton of the molecular capping layer (characterized by the same parameters as previously), we consider a silver rod of length $L$ = 155 nm.

In Figure 6a we show the calculated spectra at different beam positions along the antenna, as marked by the crosses in the schematic. When the beam is close to the antenna apexes, we excite the dipolar plasmon resonance around 1.8 eV. Interestingly, the spectra exhibit the Fano-like feature arising due to the plasmon-exciton coupling at both apexes, even when the electron beam passes close to the uncovered rod apex. For comparison, we show in Figure 6b the spectra for the situation when only the molecular cap is present, exhibiting an excitonic peak only for the beam positions close to the cap.

Most importantly, the Fano feature in the spectra calculated for the antenna-cap system is also present when the beam is probing the uncovered rod extremity ($x$ < 0 nm, Figure 6a), that is, at rather large distances from the excitonic cap. In comparison, the EEL spectra of the bare molecular cap at positons $x$ < 0 nm are more than a factor of $10^2$ smaller (Figure 6b) and thus undetectable. The plasmonic (or in general polaritonic) field thus offers a possibility for ultradistant remote sensing with EELS.

To discuss more quantitatively the spectral contrast enhancement obtained with the plasmonic antenna, we plot in Figure 6c the EEL spectra for beam positions at the antenna apexes (positions marked by colored crosses in the schematics of Figure 6a,b). For a beam position close to the cap, we observe

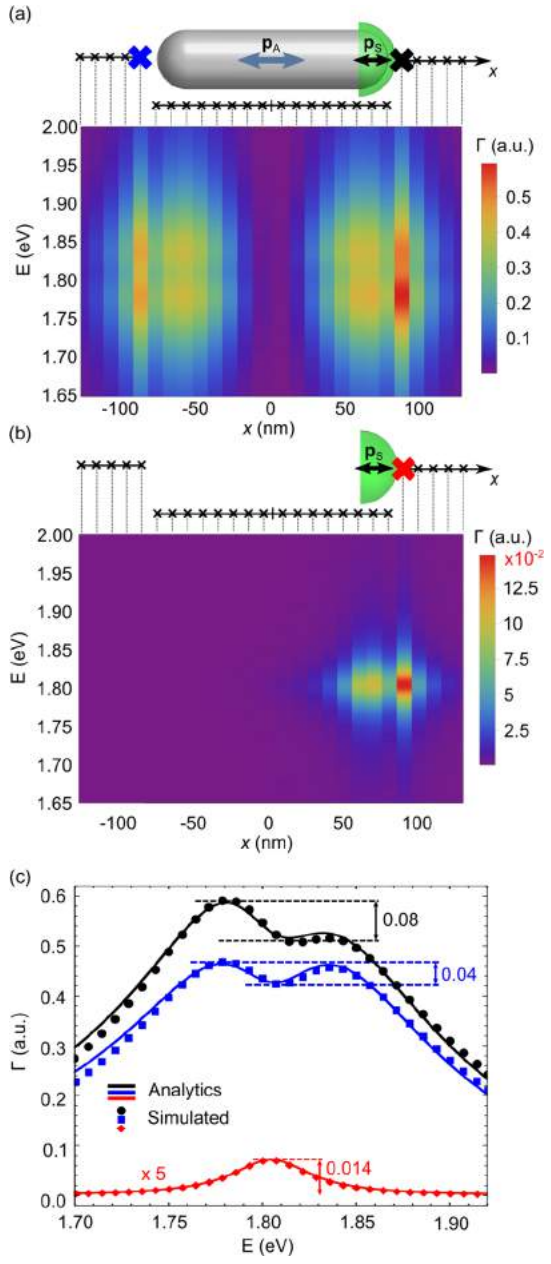


**Figure 6. (a) EELS scan along a silver antenna of length $L$ = 155 nm with an excitonic cap placed as shown in the schematic. (b) The same calculation as in panel a but without the antenna. Notice much lower values of the EELS intensity. (c) Spectra for the beam positions are denoted by the colored crosses in the schematic: ($L$/2 + 10 nm, 0) in black, (−$L$/2 − 10 nm, 0) in blue, and ($L$/2 + 10 nm, 0) in red (calculated without the antenna, multiplied by 5). The points represent numerically calculated data, the continuous lines are obtained from fitting of the analytical model of the coupled dipoles as depicted in the schematic of panel a. The response of the bare excitonic cap (red) was fitted to eq 11 considering $\alpha_A$ = 0. The fitting parameters are provided in the Methods section.**

that the EEL contrast is more than five times larger when the cap is placed onto the plasmonic antenna (compare black and red spectral points in Figure 6c). However, as discussed above, the excitonic fingerprint is also clearly visible in the spectrum when the electron beam passes close to the uncovered apex



DOI: 10.1021/acsnano.8b01481
ACS Nano XXXX, XXX, XXX–XXX

(blue points), whereas the uncoupled excitonic cap is undetectable for the same beam position.

We also observe a slight variation in the spectral shape of the Fano-like coupling feature (compare the black and blue spectra in Figure 6c). When the beam is close to the molecular cap, it efficiently excites both the antenna and the molecular sample and the calculated spectra can be nicely fitted by the coupled dipole model in eq 1 (black curve, see Methods for the fitting details). On the other hand, for the beam placed at the uncovered antenna tip, we excite mainly the plasmon and the direct excitation of the molecular cap is negligible (to fit the blue curve, we use eq 12 of Methods).

## CONCLUSIONS

In summary, we studied the electromagnetic coupling in a molecule−antenna system with an electron beam and described the involved physical mechanisms. By positioning the electron beam at specific positions along the antenna, we can effectively change the coupling in the system and probe either the uncoupled or the coupled sample-antenna system. The implementation of this electron beam probing thus allows for exploring fundamental aspects of Fano-like and strong coupling between polaritons and either excitons or vibrations. Together with high-resolution imaging, STEM-EELS will be capable of providing detailed spectral and structural information on a complex interacting system.

Furthermore, polariton-molecule coupling in EELS offers a significant enhancement of the loss signal from molecules and enables fully remote sensing, which is important especially for sensitive organic specimens. The coupling phenomena could also appear naturally in exploring catalytic reactions on metallic surfaces or small amounts of organic molecules, where both the signal enhancement and the remote sensing capability is crucial. All these perspectives make surface-enhanced EELS a powerful and promising tool for spectroscopic probing of molecules.

## METHODS

**Dielectric Response of the Studied Systems.** The dielectric response of silver in the rods is approximated by the Drude dielectric function

$$\varepsilon_{\mathrm{Ag}} = \varepsilon_\infty - \frac{\omega_\mathrm{p}^2}{\omega^2 + \mathrm{i}\gamma\omega} \tag{2}$$

where $\varepsilon_\infty = 3.3$ is the background permittivity of silver, $\omega_\mathrm{p} = 9.3$ eV the plasma frequency, and $\gamma = 22$ meV the damping parameter.[80] The dielectric response of the molecular sample is modeled by the Lorentz−Drude dielectric function

$$\varepsilon_\mathrm{s} = \varepsilon_{\infty,\mathrm{s}} + \frac{f_\mathrm{s}\omega_\mathrm{s}^2}{\omega_\mathrm{s}^2 - \omega^2 - \mathrm{i}\gamma_\mathrm{s}\omega} \tag{3}$$

where the sample exhibits either excitonic transitions in the visible or vibrational modes in the infrared spectral range at the energy $\omega_\mathrm{s}$. $\varepsilon_{\infty,\mathrm{s}}$ is the background permittivity, $f_\mathrm{s}$ is the oscillator strength, and $\gamma_\mathrm{s}$ is the damping.

h-BN exhibits anisotropic behavior and can be described by a diagonal dielectric tensor[37,73] $\hat{\varepsilon} = (\varepsilon_\perp,\varepsilon_\perp,\varepsilon_\parallel)$ with components

$$\varepsilon_{\perp/\parallel} = \varepsilon_{\infty,\perp/\parallel}\left(1 + \frac{\omega_{\mathrm{LO},\perp/\parallel}^2 - \omega_{\mathrm{TO},\perp/\parallel}^2}{\omega_{\mathrm{LO},\perp/\parallel}^2 - \omega^2 - \mathrm{i}\gamma_{\perp/\parallel}\omega}\right) \tag{4}$$

where the background permittivity $\varepsilon_{\infty,\perp/\parallel} = 4.9/2.95$, LO and TO energies read $\omega_{\mathrm{LO},\perp/\parallel} = 200.1/102.3$ meV and $\omega_{\mathrm{TO},\perp/\parallel} = 198.6/94.2$ meV, and the damping is $\gamma_{\perp/\parallel} = 0.87/0.25$ meV. However, the anisotropy and complex hyperbolic nature of h-BN phonon polaritons[38,55] in this case does not significantly influence the coupling, and the spectral response is nearly identical as for an isotropic antenna with $\hat{\varepsilon} = (\varepsilon_\perp,\varepsilon_\perp,\varepsilon_\perp)$.

**Calculation of Electron Energy Loss Spectra.** We use classical dielectric theory to calculate EEL spectra.[63,64] We assume that the induced electric field, originating from a response of the antenna−molecule system to the incident electromagnetic field of the electron beam, acts back on the beam, thus causing an energy loss which reveals the energy and strength of the excitations induced in the system. The electron beam is represented by a straight line current, implying that we are working within the nonrecoil approximation. For an electron moving along the $z$ axis, the EEL probability $\Gamma(\omega)$ of losing an energy $\omega$ (unless otherwise specified, we are using Hartree atomic units (a.u.) for expressing and plotting $\Gamma$) is given by

$$\Gamma(\omega, x_\mathrm{b}, y_\mathrm{b}) = \frac{1}{\pi\omega}\int_{-\infty}^{\infty} \mathrm{Re}[E_z^{\mathrm{ind}}(\omega, x_\mathrm{b}, y_\mathrm{b}, z)\, \mathrm{e}^{-\mathrm{i}\omega z/v}]\, \mathrm{d}z \tag{5}$$

where $E_z^{\mathrm{ind}}$ is the $z$ component of the electric field evaluated along the electron trajectory. $v = 0.446\ c$ is the electron speed (corresponding to an accelerating voltage 60 kV), with $c$ being the speed of light in vacuum. To calculate the energy loss probability $\Gamma$ we find the induced electric field, either analytically or numerically. The loss probability essentially depends on the so-called impact parameter, which is given by the distance of the beam position $(x_\mathrm{b},y_\mathrm{b})$ relative to the origin.

In a general geometrical arrangement, the induced electric field coming from the interaction of a fast electron and a nanostructure can be found by solving Maxwell's equations numerically. We performed simulations in the commercial software Comsol Multiphysics implementing the finite element method in the frequency domain and followed the same procedure as reported previously.[55,81,82]

**Coupled Dipole Model.** The antenna (A) and the excitonic sample (S) are replaced by two point dipoles situated at positions $(x_{\mathrm{A/S}},0,0)$ and for simplicity, we consider the electron beam passing at the origin, that is, $x_\mathrm{b} = y_\mathrm{b} = 0$. The dipoles are characterized by means of their polarizability tensor, $\overleftrightarrow{\alpha}_{\mathrm{A/S}}$. The dipole moment induced by the external field $\mathbf{E}^{\mathrm{tot,A/S}}$ at the dipole position is then $\mathbf{p}_{\mathrm{A/S}} = \overleftrightarrow{\alpha}_{\mathrm{A/S}}\mathbf{E}^{\mathrm{tot,A/S}}$ for the antenna and the sample, respectively. In the considered geometrical arrangement, the antenna is preferentially polarized along the $x$ direction. We therefore consider that the antenna polarizability tensor has a single nonzero component: $\alpha_{\mathrm{A},xx} = \alpha_\mathrm{A}$ and assume the sample polarizability $\alpha_\mathrm{S}$ to be isotropic. The polarizabilities have Lorentzian line shape: $\alpha_{\mathrm{A/S}} = F_{\mathrm{A/S}}\Omega_{\mathrm{A/S}}^2/(\Omega_{\mathrm{A/S}}^2 - \omega^2 - \mathrm{i}\kappa_{\mathrm{A/S}}\omega)$ where $\Omega_{\mathrm{A/S}}$ is the resonance frequency, $\kappa_{\mathrm{A/S}}$ is the damping parameter, and $F_{\mathrm{A/S}}$ is the oscillator strength associated with the uncoupled antenna and the sample, respectively. Due to the symmetry (see Figure 1a), the dipole moments will read $\mathbf{p}_{\mathrm{A/S}} = (p_{x,\mathrm{A}}, 0, 0)$ and $\mathbf{p}_\mathrm{S} = (p_{x,\mathrm{S}}, 0, p_{z,\mathrm{S}})$.

The field driving each dipole is the sum of the field of the electron beam and the field produced by the other dipole[18] $\mathbf{E}^{\mathrm{tot,A/S}} = \mathbf{E}^{\mathrm{A/S}} + \mathbf{E}^{\mathrm{SA/AS}}$, where the field of the moving electron at the dipoles' positions is[64]

$$\mathbf{E}^{\mathrm{A/S}}(x_{\mathrm{A/S}}, 0, \omega) = \left(-\frac{2\omega}{v^2\gamma_\mathrm{L}}K_1\left(\frac{\omega x_{\mathrm{A/S}}}{v\gamma_\mathrm{L}}\right), 0, \frac{\mathrm{i}2\omega}{v^2\gamma_\mathrm{L}^2}K_0\left(\frac{\omega x_{\mathrm{A/S}}}{v\gamma_\mathrm{L}}\right)\right) \tag{6}$$

where $\gamma_\mathrm{L} = 1/\sqrt{1 - v^2/c^2}$ is the Lorentz contraction factor and $K_m$ are the modified Bessel functions of the second kind of order $m$. The interaction field coming from the other dipole (sample acting on the antenna and reversely) in the considered symmetry retains only the $x$ component and is expressed as

$$\mathbf{E}^{\mathrm{SA/AS}} = (p_x^{\mathrm{S/A}}G, 0, 0) \tag{7}$$

where



DOI: 10.1021/acsnano.8b01481
ACS Nano XXXX, XXX, XXX−XXX

$$G = \frac{2\exp(i\omega x_{SA}/c)}{x_{SA}^2}\left(\frac{1}{x_{SA}} - \frac{i\omega}{c}\right) \quad (8)$$

is the $xx$ component of the Green's dyadic, simplified for the particular geometrical arrangement.[83] $x_{SA}$ is an effective distance between the dipoles and for perfect point-like particles, it is $x_{SA} = |x_A - x_S|$. We recast the expression for the $x$ component of the dipole moments:

$$p_x^{A/S} = \alpha_{A/S}(E_x^{A/S} + p_x^{S/A}G) \quad (9)$$

Equation 9 represents a self-consistent system of equations, which yields the solution:

$$p_x^{A/S} = \alpha_{A/S}\frac{E_x^{A/S} + \alpha_{S/A}GE_x^{S/A}}{1 - \alpha_A\alpha_S G^2} \quad (10)$$

The equation above involves infinite number of scattering events between the antenna and the sample. Furthermore, the sample can show a $z$ component of the dipole moment $p_z^S = \alpha_S E_z^S$, which is not influenced by the antenna. Nevertheless, this contribution can be neglected for small sample's oscillator strength $F_S$ ($F_S \ll F_A$).

The energy loss probability coming from the excitation of the antenna and sample dipoles[51,84]

$$\begin{aligned}\Gamma(\omega) &= \frac{1}{\pi}\mathrm{Im}[p_x^A E_x^{A,*}] + \frac{1}{\pi}\mathrm{Im}[p_x^S E_x^{S,*} + p_z^S E_z^{S,*}] \\ &= \frac{1}{\pi}\mathrm{Im}\left[\frac{\alpha_A (E_x^A)^2}{1 - \alpha_A\alpha_S G^2}\right] + \frac{1}{\pi}\mathrm{Im}\left[\frac{2\alpha_A G\alpha_S E_x^A E_x^S}{1 - \alpha_A\alpha_S G^2}\right] \\ &\quad + \frac{1}{\pi}\mathrm{Im}\left[\frac{\alpha_S (E_x^S)^2}{1 - \alpha_A\alpha_S G^2} + \alpha_S |E_z^S|^2\right] \\ &= \Gamma_A + \Gamma_{AS} + \Gamma_S \end{aligned} \quad (11)$$

The loss probability strongly depends on the external electric field produced by the electron at the antenna and the sample positions, respectively, which influences the relative strength of the terms $\Gamma_A$, $\Gamma_{AS}$, and $\Gamma_S$. The latter two terms are negligible when the sample is either far from the probe or weakly polarizable compared to the antenna. The spectral shape is then properly described by $\Gamma_A$:

$$\Gamma_{x_A<x_S} \approx \Gamma_A = \frac{1}{\pi}\mathrm{Im}\left[\frac{\alpha_A (E_x^A)^2}{1 - \alpha_A\alpha_S G^2}\right] \quad (12)$$

On the other hand, for a strongly excited sample, eq 11 simplifies to the approximate expression given in eq 1, where we assumed the antenna polarizability $\alpha_A$ to be much larger than the sample polarizability $\alpha_S$ and omitted $\Gamma_S$ in eq 11.

**Modeling of the Signal Decay.** The uncoupled molecular shell is replaced by a homogeneously polarizable dipole. In such a case, the peak height (intensity) follows from eq 11, setting $\alpha_A = 0$[85]

$$I_{dipole,S}(b) \propto \frac{1}{\gamma_L^2}K_0^2\left(\frac{\omega(b + b_{dip,S})}{v\gamma_L}\right) + K_1^2\left(\frac{\omega(b + b_{dip,S})}{v\gamma_L}\right) \quad (13)$$

with the beam passing at the position $(L/2 + b,0)$ and the dipole located at the effective distance $(L/2 - b_{dip,S},0)$, which approximately corresponds to center of mass of the excited sample volume. We found $b_{dip,ex}$ = 8 nm for the excitonic sample, $b_{dip,PMMA}$ = 20 nm for the PMMA sample, and $b_{dip,CBP}$ = 15 nm for the CBP molecules to reproduce the bare sample decay (red curves in Figure 5c,f,i). The PMMA and CBP dipoles are placed farther due to the larger shell volume excited in the IR. The decay of the spectral contrast in the coupled case approximately follows the signal decay of the bare antenna (see Figure S8). The antennas are preferentially polarized along the $x$ direction, which retains only the second term of eq 13. The decay of the contrast for the short antennas then reads:

$$I_{dipole,A}(b) \propto K_1^2\left(\frac{\omega(b + b_{dip,S})}{v\gamma_L}\right) \quad (14)$$

where the dipole is placed at the antenna's center of mass. The long IR antenna is described by a line charge distribution,[78] which can be approximated for the dipolar plasmon as $\tau(x) = \tau_0 x$ for $-L/2 < x < L/2$ and $\tau(x) = 0$ otherwise. In the nonretarded approximation, we obtain the following expression for the intensity of the antenna peak as a function of the beam position:[86,87]

$$I_A(b) \propto \left|\int_0^L dx'(x' - L/2)K_0\left(\frac{\omega(x' + b)}{v}\right)\right|^2 \quad (15)$$

**Fitting Calculated Data to the Coupled Dipole Model.** We first find the antenna and the sample polarizabilities, $\alpha_{A/S}$, from spectra calculated for the antenna covered by the nonresonant sample (described by $\varepsilon_s = \varepsilon_{\infty,s}$ = 1.69) and the bare sample. We fit these spectra by eq 11, considering either $\alpha_S = 0$ or $\alpha_A = 0$, respectively (decoupled antenna or sample excitation). The antenna and the sample dipoles are placed at positions $x_{A/S,0}$, which we estimate as fixed parameters. The red line in Figure 6c represents such fit for the bare excitonic cap. The calculated parameters for the polarizabilities are then used in eq 1 and eq12 and we fit the distances $x_{A/S/SA}$. The fitted values of $x_{A/S}$ approximately correspond to the center of mass of the excited antenna and sample volume.

The black and blue spectra in Figure 1d exhibit an almost symmetric Fano-dip, which would be in optical spectroscopy a signature of nearly matching energies of the uncoupled antenna resonance and the excitonic transition. However, according to Table 1 we find significant blueshift of 36 meV (detuning) between the bare antenna and the sample peak positions $\Omega_{A/S}$, which indeed results in an asymmetric Fano feature in the optical spectra (Figure S2). The general spectral shape (1) of EEL probability can thus produce a symmetric feature for a detuned system and vice versa.

**Table 1. Oscillator Parameters and the Fitted Antenna (A) and Sample (S) Dipole Distances Obtained from Analytical Modeling in Figures 1d and 6c**

| parameter | Figure 1d | Figure 6c |
|---|---|---|
| $F_A$ (a.u.) | $2.51 \times 10^9$ | $3.32 \times 10^9$ |
| $\Omega_A$ (eV) | 1.84 | 1.817 |
| $\kappa_A$(meV) | 169 | 175 |
| $x_{A,0}$ (nm) | 82.5 | 87.5 |
| $F_S$ (a.u.) | $1.18 \times 10^6$ | 98561 |
| $\Omega_S$ (eV) | 1.804 | 1.805 |
| $\kappa_S$ (meV) | 53 | 52 |
| $x_{S,0}$ (nm) | 40 | 15 |
| | | black/blue sp. |
| $x_A$ (nm) | 83 | 87/90 |
| $x_S$ (nm) | 48 | 20/NA |
| $x_{SA}$ (nm) | 79 | 63/61 |

**Evaluation of Strong Coupling.** We first calculate spectra for the uncoupled antenna covered by the nonresonant dielectric layer and the excitonic shell corresponding to each antenna length. We then fit the spectra as described in the previous section to obtain the oscillator parameters for the uncoupled antenna and the sample. With the fixed oscillator parameters, we fit the spectra calculated for the coupled antenna–molecule system by eq 1 with $x_{SA}$ as a free parameter. The coupling gives rise to two new eigenmodes, whose energies are split according to[24,31]

$$\omega_\pm = \mathrm{Re}\left[\frac{\Omega_A + \Omega_S}{2} \pm \frac{1}{2}\sqrt{4|g|^2 + \left[(\Omega_A - \Omega_S) + \frac{i(\kappa_S - \kappa_A)}{2}\right]^2}\right] \quad (16)$$

where $g$ is the interaction coupling strength between the oscillators, which in general depends on oscillator strengths, damping in the system, and effective mode volume. For the particular parameters used in our coupled-dipole model, we find an approximate expression which



DOI: 10.1021/acsnano.8b01481
ACS Nano XXXX, XXX, XXX–XXX

holds for small oscillators' damping and close to zero detuning ($\Omega_A \cong \Omega_S \cong \Omega_0$): $g \sim \Omega_0\sqrt{F_A F_S}/x_{SA}^3$. The strong coupling is reached, when the energy difference in eq 16 is larger than the width of the hybridized modes, that is, if $|g|/|\kappa_A + \kappa_S| > 0.25$ holds.

For the dipolar antenna mode and zero detuning, we obtain the coupling strength $2g_1 = 72$ meV and a value of $|g_1|/|\kappa_A + \kappa_S| = 0.16 < 0.25$ (weak coupling). However, for the first dark antenna mode, the strong coupling criterion is just above the threshold as $|g_2|/|\kappa_A + \kappa_S| = 0.26 > 0.25$. Although the coupling strength $2g_2 = 52$ meV for the dark antenna mode is smaller than for the bright dipolar mode, the smaller damping of the dark mode enables the system to enter the strong coupling regime (compare fwhm in Figures 2a and 1b).

## ASSOCIATED CONTENT

### Supporting Information

The Supporting Information is available free of charge on the ACS Publications website at DOI: 10.1021/acsnano.8b01481.

Additional Figures: EEL spectra showing excitation of higher-order longitudinal and transverse modes (S1), optical spectra of bare and covered antennas in visible (S2) and IR (S4), coupling of the excitonic layer with higher-order modes of longer antennas (S3), EEL spectrum of the IR plasmonic antenna with the PMMA cap (S5), influence of finite spectral resolution on the EEL spectrum in visible (S6), EEL linescan along the excitonic shell (S7), comparison of the signal decay dependence for coupled antenna−molecule systems vs uncoupled antennas (S8) (PDF)

## AUTHOR INFORMATION


### Corresponding Authors

*E-mail: aizpurua@ehu.eus.

*E-mail: r.hillenbrand@nanogune.eu.

### ORCID

Andrea Konečná: 0000-0002-7423-5481

Javier Aizpurua: 0000-0002-1444-7589

Rainer Hillenbrand: 0000-0002-1904-4551


### Notes

The authors declare no competing financial interest.

## ACKNOWLEDGMENTS

This work is supported by the Spanish Ministry of Economy, Industry, and Competitiveness (National Projects MAT2015-65525-R, FIS2016-80174-P, and the Project MDM-2016-0618 of the Maria de Maeztu Units of Excellence Programme). A.K. further acknowledges Thermo Fisher Scientific and Czechoslovak Microscopic Society scholarship for young researchers.

## REFERENCES


(1) Li, Z. Q.; Henriksen, E. A.; Jiang, Z.; Hao, Z.; Martin, M. C.; Kim, P.; Stormer, H. L.; Basov, D. N. Dirac Charge Dynamics in Graphene by Infrared Spectroscopy. *Nat. Phys.* **2008**, *4*, 532−535.

(2) Eberlein, T.; Bangert, U.; Nair, R. R.; Jones, R.; Gass, M.; Bleloch, A. L.; Novoselov, K. S.; Geim, A.; Briddon, P. R. Plasmon Spectroscopy of Free-Standing Graphene Films. *Phys. Rev. B: Condens. Matter Mater. Phys.* **2008**, *77*, 233406.

(3) Hildebrandt, P.; Stockburger, M. Surface-Enhanced Resonance Raman Spectroscopy of Rhodamine 6G Adsorbed on Colloidal Silver. *J. Phys. Chem.* **1984**, *88*, 5935−5944.

(4) Xu, H.; Bjerneld, E. J.; Käll, M.; Börjesson, L. Spectroscopy of Single Hemoglobin Molecules by Surface Enhanced Raman Scattering. *Phys. Rev. Lett.* **1999**, *83*, 4357−4360.

(5) Wojs, A.; Hawrylak, P.; Fafard, S.; Jacak, L. Electronic Structure and Magneto-Optics of Self-Assembled Quantum Dots. *Phys. Rev. B: Condens. Matter Mater. Phys.* **1996**, *54*, 5604−5608.

(6) Mićić, O. I.; Cheong, H. M.; Fu, H.; Zunger, A.; Sprague, J. R.; Mascarenhas, A.; Nozik, A. J. Size-Dependent Spectroscopy of InP Quantum Dots. *J. Phys. Chem. B* **1997**, *101*, 4904−4912.

(7) Khanikaev, A. B.; Mousavi, S. H.; Tse, W.-K.; Kargarian, M.; MacDonald, A. H.; Shvets, G. Photonic Topological Insulators. *Nat. Mater.* **2013**, *12*, 233−239.

(8) Uoyama, H.; Goushi, K.; Shizu, K.; Nomura, H.; Adachi, C. Highly Efficient Organic Light-Emitting Diodes from Delayed Fluorescence. *Nature* **2012**, *492*, 234−238.

(9) Anger, P.; Bharadwaj, P.; Novotny, L. Enhancement and Quenching of Single-Molecule Fluorescence. *Phys. Rev. Lett.* **2006**, *96*, 113002.

(10) Hendra, P. J.; Stratton, P. M. Laser-Raman Spectroscopy. *Chem. Rev.* **1969**, *69*, 325−344.

(11) Hollas, J. M. *Modern Spectroscopy*; John Wiley & Sons, 2004.

(12) Pelton, M.; Aizpurua, J.; Bryant, G. Metal-Nanoparticle Plasmonics. *Laser Photonics Rev.* **2008**, *2*, 136−159.

(13) Moskovits, M. Surface-Enhanced Spectroscopy. *Rev. Mod. Phys.* **1985**, *57*, 783−826.

(14) Zhang, Y.; Meng, Q.-S.; Zhang, L.; Luo, Y.; Yu, Y.-J.; Yang, B.; Zhang, Y.; Esteban, R.; Aizpurua, J.; Luo, Y.; Yang, J.-L.; Dong, Z.-C.; Hou, J. G. Sub-Nanometre Control of the Coherent Interaction between a Single Molecule and a Plasmonic Nanocavity. *Nat. Commun.* **2017**, *8*, 15225.

(15) Zhang, R.; Zhang, Y.; Dong, Z.; Jiang, S.; Zhang, C.; Chen, L.; Zhang, L.; Liao, Y.; Aizpurua, J.; Luo, Y.; Yang, J.; Hou, J. Chemical Mapping of a Single Molecule by Plasmon-Enhanced Raman Scattering. *Nature* **2013**, *498*, 82−86.

(16) Neubrech, F.; Pucci, A.; Cornelius, T. W.; Karim, S.; García-Etxarri, A.; Aizpurua, J. Resonant Plasmonic and Vibrational Coupling in a Tailored Nanoantenna for Infrared Detection. *Phys. Rev. Lett.* **2008**, *101*, 157403.

(17) Neuman, T.; Huck, C.; Vogt, J.; Neubrech, F.; Hillenbrand, R.; Aizpurua, J.; Pucci, A. Importance of Plasmonic Scattering for an Optimal Enhancement of Vibrational Absorption in SEIRA with Linear Metallic Antennas. *J. Phys. Chem. C* **2015**, *119*, 26652−26662.

(18) Adato, R.; Yanik, A. A.; Amsden, J. J.; Kaplan, D. L.; Omenetto, F. G.; Hong, M. K.; Erramilli, S.; Altug, H. Ultra-Sensitive Vibrational Spectroscopy of Protein Monolayers with Plasmonic Nanoantenna Arrays. *Proc. Natl. Acad. Sci. U. S. A.* **2009**, *106*, 19227−19232.

(19) Dong, L.; Yang, X.; Zhang, C.; Cerjan, B.; Zhou, L.; Tseng, M. L.; Zhang, Y.; Alabastri, A.; Nordlander, P.; Halas, N. J. Nanogapped Au Antennas for Ultrasensitive Surface-Enhanced Infrared Absorption Spectroscopy. *Nano Lett.* **2017**, *17*, 5768−5774.

(20) Vasa, P.; Wang, W.; Pomraenke, R.; Lammers, M.; Maiuri, M.; Manzoni, C.; Cerullo, G.; Lienau, C. Real-Time Observation of Ultrafast Rabi Oscillations between Excitons and Plasmons in Metal Nanostructures with J-Aggregates. *Nat. Photonics* **2013**, *7*, 128.

(21) Manjavacas, A.; de Abajo, F. J. G.; Nordlander, P. Quantum Plexcitonics: Strongly Interacting Plasmons and Excitons. *Nano Lett.* **2011**, *11*, 2318−2323.

(22) Antosiewicz, T. J.; Apell, S. P.; Shegai, T. Plasmon-Exciton Interactions in a Core-Shell Geometry: From Enhanced Absorption to Strong Coupling. *ACS Photonics* **2014**, *1*, 454−463.

(23) Chikkaraddy, R.; de Nijs, B.; Benz, F.; Barrow, S. J.; Scherman, O. A.; Rosta, E.; Demetriadou, A.; Fox, P.; Hess, O.; Baumberg, J. J. Single-Molecule Strong Coupling at Room Temperature in Plasmonic Nanocavities. *Nature* **2016**, *535*, 127−130.

(24) Törmä, P.; Barnes, W. L. Strong Coupling Between Surface Plasmon Polaritons and Emitters: A Review. *Rep. Prog. Phys.* **2015**, *78*, 013901.

(25) Wurtz, G. A.; Evans, P. R.; Hendren, W.; Atkinson, R.; Dickson, W.; Pollard, R. J.; Zayats, A. V.; Harrison, W.; Bower, C. Molecular Plasmonics with Tunable Exciton−Plasmon Coupling Strength in J-Aggregate Hybridized Au Nanorod Assemblies. *Nano Lett.* **2007**, *7*, 1297−1303.




DOI: 10.1021/acsnano.8b01481
*ACS Nano* XXXX, XXX, XXX−XXX

(26) Wiederrecht, G. P.; Wurtz, G. A.; Hranisavljevic, J. Coherent Coupling of Molecular Excitons to Electronic Polarizations of Noble Metal Nanoparticles. *Nano Lett.* **2004**, *4*, 2121−2125.
(27) Fofang, N. T.; Park, T.-H.; Neumann, O.; Mirin, N. A.; Nordlander, P.; Halas, N. J. Plexcitonic Nanoparticles: Plasmon-Exciton Coupling in Nanoshell-J-Aggregate Complexes. *Nano Lett.* **2008**, *8*, 3481−3487.
(28) Bellessa, J.; Bonnand, C.; Plenet, J. C.; Mugnier, J. Strong Coupling between Surface Plasmons and Excitons in an Organic Semiconductor. *Phys. Rev. Lett.* **2004**, *93*, 036404.
(29) Schlather, A. E.; Large, N.; Urban, A. S.; Nordlander, P.; Halas, N. J. Near-Field Mediated Plexcitonic Coupling and Giant Rabi Splitting in Individual Metallic Dimers. *Nano Lett.* **2013**, *13*, 3281−3286.
(30) Zengin, G.; Wersäll, M.; Nilsson, S.; Antosiewicz, T. J.; Käll, M.; Shegai, T. Realizing Strong Light-Matter Interactions between Single-Nanoparticle Plasmons and Molecular Excitons at Ambient Conditions. *Phys. Rev. Lett.* **2015**, *114*, 157401.
(31) Melnikau, D.; Esteban, R.; Savateeva, D.; Sánchez-Iglesias, A.; Grzelczak, M.; Schmidt, M. K.; Liz-Marzán, L. M.; Aizpurua, J.; Rakovich, Y. P. Rabi Splitting in Photoluminescence Spectra of Hybrid Systems of Gold Nanorods and J-Aggregates. *J. Phys. Chem. Lett.* **2016**, *7*, 354−362.
(32) Artuso, R. D.; Bryant, G. W. Optical Response of Strongly Coupled Quantum Dot-Metal Nanoparticle Systems: Double Peaked Fano Structure and Bistability. *Nano Lett.* **2008**, *8*, 2106−2111.
(33) Gómez, D. E.; Vernon, K. C.; Mulvaney, P.; Davis, T. J. Surface Plasmon Mediated Strong Exciton-Photon Coupling in Semiconductor Nanocrystals. *Nano Lett.* **2010**, *10*, 274−278.
(34) Wang, H.; Wang, H.-Y.; Toma, A.; Yano, T.-a.; Chen, Q.-D.; Xu, H.-L.; Sun, H.-B.; Proietti Zaccaria, R. Dynamics of Strong Coupling between CdSe Quantum Dots and Surface Plasmon Polaritons in Subwavelength Hole Array. *J. Phys. Chem. Lett.* **2016**, *7*, 4648−4654.
(35) Wei, J.; Jiang, N.; Xu, J.; Bai, X.; Liu, J. Strong Coupling between ZnO Excitons and Localized Surface Plasmons of Silver Nanoparticles Studied by STEM-EELS. *Nano Lett.* **2015**, *15*, 5926−5931.
(36) Santhosh, K.; Bitton, O.; Chuntonov, L.; Haran, G. Vacuum Rabi Splitting In a Plasmonic Cavity at the Single Quantum Emitter Limit. *Nat. Commun.* **2016**, *7*, 11823.
(37) Caldwell, J. D.; Kretinin, A. V.; Chen, Y.; Giannini, V.; Fogler, M. M.; Francescato, Y.; Ellis, C. T.; Tischler, J. G.; Woods, C. R.; Giles, A. J.; Hong, M.; Watanabe, K.; Taniguchi, T.; Maier, S. A.; Novoselov, K. S. Sub-Diffractional Volume-Confined Polaritons in the Natural Hyperbolic Material Hexagonal Boron Nitride. *Nat. Commun.* **2014**, *5*, 5221.
(38) Alfaro-Mozaz, F.; Alonso-González, P.; Vélez, S.; Dolado, I.; Autore, M.; Mastel, S.; Casanova, F.; Hueso, L.; Li, P.; Nikitin, A.; Hillenbrand, R. Nanoimaging of Resonating Hyperbolic Polaritons in Linear Boron Nitride Antennas. *Nat. Commun.* **2017**, *8*, 15624.
(39) Autore, M.; Li, P.; Dolado, I.; Alfaro-Mozaz, F. J.; Esteban, R.; Atxabal, A.; Casanova, F.; Hueso, L. E.; Alonso-González, P.; Aizpurua, J.; Nikitin, A. Y.; Vélez, S.; Hillenbrand, R. Boron Nitride Nanoresonators for Phonon-Enhanced Molecular Vibrational Spectroscopy at the Strong Coupling Limit. *Light: Sci. Appl.* **2017**, *7*, e17172.
(40) Egerton, R. F. *Electron Energy-Loss Spectroscopy in the Electron Microscope*, 3rd ed.; Springer: New York, 2011.
(41) Batson, P. Simultaneous STEM Imaging and Electron Energy-Loss Spectroscopy with Atomic-Column Sensitivity. *Nature* **1993**, *366*, 727−728.
(42) Wu, Y.; Li, G.; Camden, J. P. Probing Nanoparticle Plasmons with Electron Energy Loss Spectroscopy. *Chem. Rev.* **2018**, *118*, 2994−3031.
(43) Nelayah, J.; Kociak, M.; Stéphan, O.; de Abajo, F. J. G.; Tencé, M.; Henrard, L.; Taverna, D.; Pastoriza-Santos, I.; Liz-Marzán, L. M.; Colliex, C. Mapping Surface Plasmons on a Single Metallic Nanoparticle. *Nat. Phys.* **2007**, *3*, 348−353.
(44) Collins, S. M.; Nicoletti, O.; Rossouw, D.; Ostasevicius, T.; Midgley, P. A. Excitation Dependent Fano-Like Interference Effects in Plasmonic Silver Nanorods. *Phys. Rev. B: Condens. Matter Mater. Phys.* **2014**, *90*, 155419.
(45) Schmidt, F.-P.; Ditlbacher, H.; Hohenester, U.; Hohenau, A.; Hofer, F.; Krenn, J. R. Dark Plasmonic Breathing Modes in Silver Nanodisks. *Nano Lett.* **2012**, *12*, 5780−5783.
(46) Chu, M.-W.; Myroshnychenko, V.; Chen, C. H.; Deng, J.-P.; Mou, C.-Y.; García de Abajo, F. J. Probing Bright and Dark Surface-Plasmon Modes in Individual and Coupled Noble Metal Nanoparticles Using an Electron Beam. *Nano Lett.* **2009**, *9*, 399−404.
(47) Koh, A. L.; Bao, K.; Khan, I.; Smith, W. E.; Kothleitner, G.; Nordlander, P.; Maier, S. A.; McComb, D. W. Electron Energy-Loss Spectroscopy (EELS) of Surface Plasmons in Single Silver Nanoparticles and Dimers: Influence of Beam Damage and Mapping of Dark Modes. *ACS Nano* **2009**, *3*, 3015−3022.
(48) Alber, I.; Sigle, W.; Müller, S.; Neumann, R.; Picht, O.; Rauber, M.; van Aken, P. A.; Toimil-Molares, M. E. Visualization of Multipolar Longitudinal and Transversal Surface Plasmon Modes in Nanowire Dimers. *ACS Nano* **2011**, *5*, 9845−9853.
(49) Bellido, E. P.; Zhang, Y.; Manjavacas, A.; Nordlander, P.; Botton, G. A. Plasmonic Coupling of Multipolar Edge Modes and the Formation of Gap Modes. *ACS Photonics* **2017**, *4*, 1558−1565.
(50) Barrow, S. J.; Rossouw, D.; Funston, A. M.; Botton, G. A.; Mulvaney, P. Mapping Bright and Dark Modes in Gold Nanoparticle Chains using Electron Energy Loss Spectroscopy. *Nano Lett.* **2014**, *14*, 3799−3808.
(51) Bigelow, N. W.; Vaschillo, A.; Iberi, V.; Camden, J. P.; Masiello, D. J. Characterization of the Electron- and Photon-Driven Plasmonic Excitations of Metal Nanorods. *ACS Nano* **2012**, *6*, 7497−7504.
(52) Bigelow, N. W.; Vaschillo, A.; Camden, J. P.; Masiello, D. J. Signatures of Fano Interferences in the Electron Energy Loss Spectroscopy and Cathodoluminescence of Symmetry-Broken Nanorod Dimers. *ACS Nano* **2013**, *7*, 4511−4519.
(53) Krivanek, O. L.; Lovejoy, T. C.; Murfitt, M. F.; Skone, G.; Batson, P. E.; Dellby, N. Towards Sub-10 meV Energy Resolution STEM-EELS. *J. Phys.: Conf. Ser.* **2014**, *522*, 012023.
(54) Krivanek, O. L.; Lovejoy, T. C.; Dellby, N.; Aoki, T.; Carpenter, R. W.; Rez, P.; Soignard, E.; Zhu, J.; Batson, P. E.; Lagos, M. J.; Egerton, R. F.; Crozier, P. A. Vibrational Spectroscopy in the Electron Microscope. *Nature* **2014**, *514*, 209−212.
(55) Govyadinov, A. A.; Konečná, A.; Chuvilin, A.; Vélez, S.; Dolado, I.; Nikitin, A. Y.; Lopatin, S.; Casanova, F.; Hueso, L. E.; Aizpurua, J.; Hillenbrand, R. Probing Low-Energy Hyperbolic Polaritons in van der Waals Crystals with an Electron Microscope. *Nat. Commun.* **2017**, *8*, 95.
(56) Rez, P.; Aoki, T.; March, K.; Gur, D.; Krivanek, O. L.; Dellby, N.; Lovejoy, T. C.; Wolf, S. G.; Cohen, H. Damage-Free Vibrational Spectroscopy of Biological Materials in the Electron Microscope. *Nat. Commun.* **2016**, *7*, 10945.
(57) Crozier, P. A.; Aoki, T.; Liu, Q. Detection of Water and its Derivatives on Individual Nanoparticles Using Vibrational Electron Energy-Loss Spectroscopy. *Ultramicroscopy* **2016**, *169*, 30−36.
(58) Venkatraman, K.; Rez, P.; March, K.; Crozier, P. A. The Influence of Surfaces and Interfaces on High Spatial Resolution Vibrational EELS from $SiO_2$. *Microscopy* **2018**, *67*, i14−i23.
(59) Lagos, M. J.; Trügler, A.; Hohenester, U.; Batson, P. E. Mapping Vibrational Surface and Bulk Modes in a Single Nanocube. *Nature* **2017**, *543*, 529−532.
(60) Bryant, G. W.; García de Abajo, F. J.; Aizpurua, J. Mapping the Plasmon Resonances of Metallic Nanoantennas. *Nano Lett.* **2008**, *8*, 631−636.
(61) Aizpurua, J.; Bryant, G. W.; Richter, L. J.; García de Abajo, F.; Kelley, B. K.; Mallouk, T. Optical Properties of Coupled Metallic Nanorods for Field-Enhanced Spectroscopy. *Phys. Rev. B: Condens. Matter Mater. Phys.* **2005**, *71*, 235420.
(62) Bosman, M.; Ye, E.; Tan, S. F.; Nijhuis, C. A.; Yang, J. K. W.; Marty, R.; Mlayah, A.; Arbouet, A.; Girard, C.; Han, M.-Y. Surface Plasmon Damping Quantified with an Electron Nanoprobe. *Sci. Rep.* **2013**, *3*, 1312.


DOI: 10.1021/acsnano.8b01481
*ACS Nano* XXXX, XXX, XXX−XXX

(63) Ritchie, R. H. Plasma Losses by Fast Electrons in Thin Films. *Phys. Rev.* **1957**, *106*, 874−881.
(64) García de Abajo, F. J. Optical Excitations in Electron Microscopy. *Rev. Mod. Phys.* **2010**, *82*, 209−275.
(65) Alonso-González, P.; Albella, P.; Schnell, M.; Chen, J.; Huth, F.; García-Etxarri, A.; Casanova, F.; Golmar, F.; Arzubiaga, L.; Hueso, L. E.; Aizpurua, J.; Hillenbrand, R. Resolving the Electromagnetic Mechanism of Surface-Enhanced Light Scattering at Single Hot Spots. *Nat. Commun.* **2012**, *3*, 684.
(66) Esteban, R.; Aizpurua, J.; Bryant, G. W. Strong Coupling of Single Emitters Interacting with Phononic Infrared Antennae. *New J. Phys.* **2014**, *16*, 013052.
(67) Ebbesen, T. W. Hybrid Light-Matter States in a Molecular and Material Science Perspective. *Acc. Chem. Res.* **2016**, *49*, 2403−2412.
(68) Hutchison, J. A.; Schwartz, T.; Genet, C.; Devaux, E.; Ebbesen, T. W. Modifying Chemical Landscapes by Coupling to Vacuum Fields. *Angew. Chem., Int. Ed.* **2012**, *51*, 1592−1596.
(69) Galego, J.; Garcia-Vidal, F. J.; Feist, J. Cavity-Induced Modifications of Molecular Structure in the Strong-Coupling Regime. *Phys. Rev. X* **2015**, *5*, 041022.
(70) Zengin, G.; Johansson, G.; Johansson, P.; Antosiewicz, T. J. A.; Käll, M.; Shegai, T. Approaching the Strong Coupling Limit in Single Plasmonic Nanorods Interacting with J-Aggregates. *Sci. Rep.* **2013**, *3*, 3074.
(71) Zengin, G.; Gschneidtner, T.; Verre, R.; Shao, L.; Antosiewicz, T. J.; Moth-Poulsen, K.; Käll, M.; Shegai, T. Evaluating Conditions for Strong Coupling between Nanoparticle Plasmons and Organic Dyes Using Scattering and Absorption Spectroscopy. *J. Phys. Chem. C* **2016**, *120*, 20588−20596.
(72) Caldwell, J. D.; Lindsay, L.; Giannini, V.; Vurgaftman, I.; Reinecke, T. L.; Maier, S. A.; Glembocki, O. J. Low-Loss, Infrared and Terahertz Nanophotonics Using Surface Phonon Polaritons. *Nanophotonics* **2015**, *4*, 44−68.
(73) Dai, S.; Fei, Z.; Ma, Q.; Rodin, A. S.; Wagner, M.; McLeod, A. S.; Liu, M. K.; Gannett, W.; Regan, W.; Watanabe, K.; Taniguchi, T.; Thiemens, M.; Dominguez, G.; Neto, A. H. C.; Zettl, A.; Keilmann, F.; Jarillo-Herrero, P.; Fogler, M. M.; Basov, D. N. Tunable Phonon Polaritons in Atomically Thin van der Waals Crystals of Boron Nitride. *Science* **2014**, *343*, 1125−1129.
(74) Hillenbrand, R.; Taubner, T.; Keilmann, F. Phonon-Enhanced Light−Matter Interaction at the Nanometre Scale. *Nature* **2002**, *418*, 159−162.
(75) Lourenço-Martins, H.; Kociak, M. Vibrational Surface Electron-Energy-Loss Spectroscopy Probes Confined Surface-Phonon Modes. *Phys. Rev. X* **2017**, *7*, 041059.
(76) Glaser, T.; Beck, S.; Lunkenheimer, B.; Donhauser, D.; Köhn, A.; Kröger, M.; Pucci, A. Infrared Study of the $MoO_3$ Doping Efficiency in 4,4'-bis(N-Carbazolyl)-1,1'-Biphenyl (CBP). *Org. Electron.* **2013**, *14*, 575−583.
(77) Lopatin, S.; Cheng, B.; Liu, W.-T.; Tsai, M.-L.; He, J.-H.; Chuvilin, A. Optimization of Monochromated TEM for Ultimate Resolution Imaging and Ultrahigh Resolution Electron Energy Loss Spectroscopy. *Ultramicroscopy* **2018**, *184*, 109−115.
(78) Kalousek, R.; Dub, P.; Bříinek, L.; Šikola, T. Response of Plasmonic Resonant Nanorods: An Analytical Approach to Optical Antennas. *Opt. Express* **2012**, *20*, 17916−17927.
(79) Cohen, H.; Maniv, T.; Tenne, R.; Rosenfeld Hacohen, Y.; Stephan, O.; Colliex, C. Near-Field Electron Energy Loss Spectroscopy of Nanoparticles. *Phys. Rev. Lett.* **1998**, *80*, 782−785.
(80) Hohenester, U.; Trügler, A. MNPBEM − A Matlab Toolbox for the Simulation of Plasmonic Nanoparticles. *Comput. Phys. Commun.* **2012**, *183*, 370−381.
(81) Wiener, A.; Duan, H.; Bosman, M.; Horsfield, A. P.; Pendry, J. B.; Yang, J. K. W.; Maier, S. A.; Fernández-Domínguez, A. I. Electron-Energy Loss Study of Nonlocal Effects in Connected Plasmonic Nanoprisms. *ACS Nano* **2013**, *7*, 6287−6296.
(82) Raza, S.; Stenger, N.; Pors, A.; Holmgaard, T.; Kadkhodazadeh, S.; Wagner, J. B.; Pedersen, K.; Wubs, M.; Bozhevolnyi, S. I.; Mortensen, N. A. Extremely Confined Gap Surface-Plasmon Modes Excited by Electrons. *Nat. Commun.* **2014**, *5*, 5125.
(83) Novotny, L.; Hecht, B. *Principles of Nano-Optics*; Cambridge University Press, 2012.
(84) Henrard, L.; Lambin, P. Calculation of the Energy Loss for an Electron Passing near Giant Fullerenes. *J. Phys. B: At., Mol. Opt. Phys.* **1996**, *29*, 5127−5141.
(85) Lucas, A. A.; Šunjić, M. Fast-Electron Spectroscopy of Collective Excitations in Solids. *Prog. Surf. Sci.* **1972**, *2*, 75−137.
(86) García de Abajo, F. J.; Aizpurua, J. Numerical Simulation of Electron Energy Loss near Inhomogeneous Dielectrics. *Phys. Rev. B: Condens. Matter Mater. Phys.* **1997**, *56*, 15873−15884.
(87) Boudarham, G.; Kociak, M. Modal Decompositions of the Local Electromagnetic Density of States and Spatially Resolved Electron Energy Loss Probability in Terms of Geometric Modes. *Phys. Rev. B: Condens. Matter Mater. Phys.* **2012**, *85*, 245447.


DOI: 10.1021/acsnano.8b01481
*ACS Nano* XXXX, XXX, XXX−XXX